

Article

# Enhancement of Peroxydisulfate Activation for Complete Degradation of Refractory Tetracycline by 3D Self-Supported MoS<sub>2</sub>/MXene Nanocomplex

Yuxia Song , Runhua Chen \*, Shihai Li, Shali Yu, Xiaoli Ni, Minglong Fang and Hanyun Xie

College of Life and Environmental Sciences, Central South University of Forestry and Technology, Changsha 410004, China; yuxiasong@csuft.edu.cn (Y.S.)

\* Correspondence: author's chen12@csuft.edu.cn

**Abstract:** Antibiotic abuse, particularly the excessive use of tetracycline (TC), a drug with significant environmental risk, has gravely harmed natural water bodies and even posed danger to human health. In this study, a three-dimensional self-supported MoS<sub>2</sub>/MXene nanohybrid with an expanded layer spacing was synthesized via a facile one-step hydrothermal method and used to activate peroxydisulfate (PDS) for the complete degradation of TC. The results showed that a stronger •OH signal was detected in the aqueous solution containing MoS<sub>2</sub>/MXene, demonstrating a superior PDS activation effect compared to MoS<sub>2</sub> or Ti<sub>3</sub>C<sub>2</sub>T<sub>x</sub> MXene alone. Under the conditions of a catalyst dosage of 0.4 g/L, a PDS concentration of 0.4 mM, and pH = 5.0, the MoS<sub>2</sub>/MXene/PDS system was able to fully eliminate TC within one hour, which was probably due to the presence of several reactive oxygen species (ROS) (•OH, SO<sub>4</sub><sup>•−</sup>, and O<sub>2</sub><sup>•−</sup>) in the system. The high TC degradation efficiency could be maintained under the influence of various interfering ions and after five cycles, indicating that MoS<sub>2</sub>/MXene has good anti-interference and reusability performance. Furthermore, the possible degradation pathways were proposed by combining liquid chromatography–mass spectrometry (LC-MS) data and other findings, and the mechanism of the MoS<sub>2</sub>/MXene/PDS system on the degradation process of TC was elucidated by deducing the possible mechanism of ROS generation in the reaction process. All of these findings suggest that the MoS<sub>2</sub>/MXene composite catalyst has strong antibiotic removal capabilities with a wide range of application prospects.

**Keywords:** MoS<sub>2</sub>; MXene; PDS; tetracycline; ROS**Citation:** Song, Y.; Chen, R.; Li, S.; Yu, S.; Ni, X.; Fang, M.; Xie, H.Enhancement of Peroxydisulfate Activation for Complete Degradation of Refractory Tetracycline by 3D Self-Supported MoS<sub>2</sub>/MXene Nanocomplex. *Nanomaterials* **2024**, *14*, 786. <https://doi.org/10.3390/nano14090786>

Academic Editor: Francesc Viñes Solana

Received: 15 April 2024

Revised: 26 April 2024

Accepted: 29 April 2024

Published: 30 April 2024



**Copyright:** © 2024 by the authors. Licensee MDPI, Basel, Switzerland. This article is an open access article distributed under the terms and conditions of the Creative Commons Attribution (CC BY) license (<https://creativecommons.org/licenses/by/4.0/>).

## 1. Introduction

The content of refractory and toxic antibiotics in water bodies is increasing due to the random dumping of personal care products (PPCPs), active pharmaceutical compounds, and other medical supplies in recent years, posing a serious threat to the ecological environment of natural water bodies and even human health [1,2]. Among them, tetracyclines (TCs) are widely used in medicine and animal husbandry due to their low cost and broad-spectrum activity, resulting in significant environmental risks [3,4]. It is difficult to remove TC from the environment using common methods. For instance, adsorption can merely transfer TC in water to the surface of a solid adsorbent without removing it fundamentally, while biological resistance and chemical stability would limit the biodegradation process, resulting in a low degradation efficiency (below 56%) [5,6]. Therefore, an innovative method for eliminating TC from the environment is critical.

Applying advanced oxidation processes (AOPs) to the oxidative destruction of organic compounds is a major area of current research. When compared to the traditional hydroxyl radical (•OH), the sulfate radicals (SO<sub>4</sub><sup>•−</sup>) of sulfate radical-based advanced oxidation processes (SR-AOPs) have a greater redox potential (2.5–3.1 eV vs. 1.8–2.7 eV), a longer half-life (30–40 s vs. 20 ns), a wider pH range, and higher selectivity, providing them an edge in degrading organic contaminants [7,8]. Nevertheless, only when activated under

certain conditions (such as UV light [9], ultrasound [10], carbon-based materials [11], and transition metals [12]) that peroxydisulfate (PDS) can produce reactive oxygen species (ROS), including sulfate radicals ( $\text{SO}_4^{\bullet-}$ ) and superoxide radicals ( $\text{O}_2^{\bullet-}$ ), to properly breakdown organic contaminants [13]. However, UV radiation and ultrasonic waves are limited by their high cost and low energy efficiency, while carbon-based catalysts can only adsorb organics to their surface rather than decompose them [14,15]. It has been reported that transition metals could be useful catalysts for PDS activation [7]. Generally,  $\text{Co}^{2+}$  and  $\text{Fe}^{2+}$  are the most widely utilized transition metals, and they have a high ability to activate PDS [16]. Unfortunately, limitations such as high cost and toxicity from  $\text{Co}^{2+}$  leaching and the conversion of  $\text{Fe}^{2+}$  to  $\text{Fe}^{3+}$  to produce precipitation would interfere with PDS activation, restricting the application of these two ions in practice [16,17].

Layered transition metal dichalcogenides (TMDs, generally  $\text{MoS}_2$ ) have been reported to be employed as inorganic activators or catalysts to activate PDS ( $\text{S}_2\text{O}_8^{2-}$ ) to generate ROS directly for pollutant disintegration [16,18]. Furthermore,  $\text{MoS}_2$  is an exceptional chemical reagent for effectively activating PDS, owing to its low cost, excellent chemical stability, mechanical robustness, non-toxicity/low toxicity, and flexible physical/chemical properties [19]. However, the native interlayer spacing of  $\text{MoS}_2$  is rather small (0.3 nm), limiting the capacity of ions/molecules to interact with internal S atoms and impeding the efficient activation of PDS by active surfaces and edge sites [17,20]. Therefore,  $\text{MoS}_2$  nanocomposites with an enlarged interlayer spacing are required. It has been proven that solvothermal synthesis with Mo and S precursors can produce  $\text{MoS}_2$  nanosheets with an increased interlayer spacing (0.94 nm), along with a surface-exposed plentiful active group, allowing them to exhibit stronger activity [17]. Additionally,  $\text{MoS}_2$  nanosheets are straightforward to aggregate since their intrinsic high surface energy results in a drop in electron transfer rate and surface-active sites [21]. As a result, directional growth of  $\text{MoS}_2$  on a hydrophilic, large, specific surface carrier is another effective strategy for increasing layer spacing, thereby exposing more active sites and improving its application in wastewater treatment [22]. In recent years, novel MXene materials (such as  $\text{Ti}_3\text{C}_2\text{T}_x$  MXene) have attracted extensive attention in various fields due to their excellent performance [23,24]. MXene, a two-dimensional transition metal substance consisting of selectively etched ternary nitrides or carbides, with ecologically favorable features, a large surface area, excellent chemical stability, unique metallic thermal/electrical conductivity, and hydrophilic qualities, has been widely used in sensors, lithium-ion batteries, supercapacitors, and environmental applications [25]. It is mainly composed of transition metal carbides, and the chemical formula is commonly expressed as  $\text{M}_{n+1}\text{X}_n\text{T}_x$ , where M is a transition element (e.g., V, Mo, Ti, etc.), X is C or N, and  $\text{T}_x$  stands for the surface terminations. Among the various MXene materials,  $\text{Ti}_3\text{C}_2\text{T}_x$  is the most widely used [24]. However, the fabrication of devices and functional coatings based on  $\text{Ti}_3\text{C}_2\text{T}_x$  remains challenging as they are susceptible to chemical degradation through oxidation to  $\text{TiO}_2$  [24,26,27]. In addition, the hydrothermal/solvothermal techniques that are typically used to produce MXene-based nanomaterials can accelerate MXene oxidation. It is found that  $\text{Ti}_3\text{C}_2\text{T}_x$  MXene is easily oxidized during the hydrothermal process due to the presence of dissolved oxygen, resulting in performance loss [28]. Consequently, a simple solution approach is urgently needed to completely encapsulate and anchor  $\text{MoS}_2$  nanosheets on the surface of  $\text{Ti}_3\text{C}_2\text{T}_x$  MXene to combine the useful properties of these two components into functional heterojunctions and overcome their respective deficiencies for efficient activation of PDS for catalytic degradation of TC.

In this study, we designed an effective and stable  $\text{MoS}_2/\text{MXene}$  catalyst for the successful activation of PDS to generate ROS to catalyze the breakdown of residual refractory TC in water. Furthermore,  $\text{MoS}_2$  nanoflowers were strongly coupled with  $\text{Ti}_3\text{C}_2\text{T}_x$  MXene via a well-designed one-step hydrothermal process. In this method, a new sulfur source, sodium diethyldithiocarbamate trihydrate (DDC), and a capping agent, EDTA, were used to substantially widen the interlayer spacing of the nanocomposite and to gain abundant surface-active sites, while the excellent chelating ability of DDC allowed the  $\text{MoS}_2$  precursor

to be tightly coupled to  $\text{Ti}_3\text{C}_2\text{T}_x$  MXene, thus effectively preventing the chemical reaction of  $\text{Ti}_3\text{C}_2\text{T}_x$  MXene at the initial stage of the hydrothermal reaction [23,29]. The synthesized composites were characterized and analyzed using SEM, FTIR, and XPS, and the effects of different factors on the degradation of TC in water by  $\text{MoS}_2/\text{MXene}$ -activated PDS were meticulously investigated, while also inferring the possible degradation mechanism of TC. The findings of this study will contribute to the construction of  $\text{MoS}_2$ , MXene, and their composites, as well as the production of powerful persulfate-activating catalysts, allowing for the efficient purification of refractory persistent organic pollutants in water.

## 2. Materials and Methods

### 2.1. Materials

Titanium aluminum carbide ( $\text{Ti}_3\text{AlC}_2$ ) was obtained from 11 Technology Co., Ltd. in Jilin, China. Sodium molybdate dihydrate ( $\text{Na}_2\text{MoO}_4 \cdot 2\text{H}_2\text{O}$ ), sodium diethyldithiocarbamate trihydrate (DDC), ethylenediaminetetraacetic acid (EDTA), tetracycline hydrochloride (TC), sodium persulfate ( $\text{Na}_2\text{S}_2\text{O}_8$ , peroxydisulfate (PDS)), and p-benzoquinone (BQ) were purchased from MACKLIN Biochemical Co., Ltd., Shanghai, China. Sulfuric acid ( $\text{H}_2\text{SO}_4$ ), sodium hydroxide (NaOH), lithium fluoride (LiF), anhydrous ethanol ( $\text{C}_2\text{H}_5\text{OH}$ ), sodium chloride (NaCl), sodium nitrate ( $\text{NaNO}_3$ ), sodium dihydrogen phosphate ( $\text{NaH}_2\text{PO}_4$ ), sodium carbonate ( $\text{Na}_2\text{CO}_3$ ), and tert-butyl alcohol (TBA) were purchased from Sinopharm Chemical Reagent Co., Ltd., Shanghai, China. All chemicals used are of analytical grade, and deionized water was used in all experiments.

### 2.2. Synthesis of $\text{MoS}_2/\text{MXene}$

The facile one-step hydrothermal synthesis method of  $\text{MoS}_2/\text{MXene}$  is shown in Figure 1. Firstly, the preparation of  $\text{Ti}_3\text{C}_2\text{T}_x$  MXene dispersion followed the method described in previous studies [28,30]. A standard hydrothermal procedure was used to synthesize  $\text{MoS}_2/\text{MXene}$  nanocomposites. Briefly, 0.7566 g of sodium molybdate dihydrate and 0.2 g of EDTA were dispersed in 50 mL of the pre-prepared  $\text{Ti}_3\text{C}_2\text{T}_x$  MXene dispersion, which underwent absolute ultrasonic processing for 1 h. After oscillation mixing for 0.5 h, 0.7650 g of DDC was added to the suspension with continuous mixing for 0.5 h. Subsequently, the combination was heated at  $180^\circ\text{C}$  for 24 h in a Teflon-lined hydrothermal autoclave reactor. Upon cooling the solution to room temperature naturally, the resulting precipitate was washed several times with deionized water/absolute ethanol, and then, the  $\text{MoS}_2/\text{MXene}$  complex was collected after freeze-drying under vacuum. MXene and  $\text{MoS}_2$  monomers were prepared under the same conditions for subsequent analysis and comparison as the blank control. In addition, several  $\text{MoS}_2/\text{MXene}$  samples were prepared by setting different mass ratios of  $\text{MoS}_2$  and MXene (1:1, 2:1, and 3:1).

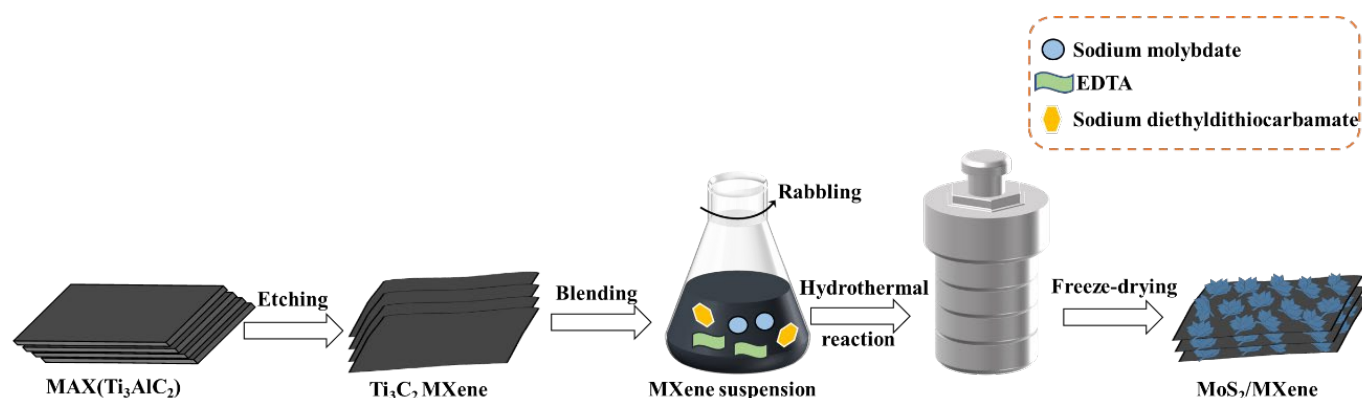


Figure 1. Schematic diagram of the synthesis of  $\text{MoS}_2/\text{MXene}$ .

### 2.3. Characterization

A variety of characterization approaches were used to observe the microscopic surface arrangement and element valence makeup of the prepared MoS<sub>2</sub>/MXene samples. The morphology and structure of different samples were observed using a scanning electron microscope (SEM; ZEISS Sigma 300, Roedermark Germany) equipped with an energy-dispersive X-ray spectrometer (EDX). The chemical bonds and surface functional groups of MoS<sub>2</sub>, MXene, and MoS<sub>2</sub>/MXene were investigated via Fourier-transform infrared spectroscopy (FTIR; Thermo Scientific Nicolet iS20, MA, USA). The surface elemental composition and chemical state were analyzed using X-ray photoelectron spectroscopy (XPS; Thermo Scientific K-Alpha, MA, USA).

### 2.4. ESR Analysis

To better illustrate the role of reactive oxygen species in the activation of PDS by MoS<sub>2</sub>/MXene, electron spin resonance (ESR) spectra were obtained using an ESR spectrometer (JESFA200, JEOL) in air, with a resonance frequency of 9225.960 MHz, a microwave power of 0.998 mW, a center field of 329.4 mT, a modulation frequency of 100 kHz, a sweep width of  $5 \times 1$  mT, a time constant of 0.03 s, and a sweep time of 30 s, and 5,5-dimethyl-1-pyrroline -N-oxide (DMPO) was used as a spin trap to capture hydroxyl radicals and generate DMPO-•OH signals using hyperfine splitting at room temperature.

### 2.5. TC Degradation Experiments

All TC degradation experiments were carried out in 150 mL Erlenmeyer flasks at 25 °C under varying experimental conditions, which included the material system (MXene only, MoS<sub>2</sub> only, and MoS<sub>2</sub>/Mxene), catalyst dosage, PDS consumption, pH, and initial concentration of TC.

Specifically, 50 mL of TC solution was placed in a 150 mL flask. After a certain amount of the catalyst material was added to the solution, which was stirred for 10 min, PDS of a certain concentration was added to initiate the degradation reaction. During the reaction process, 1.0 mL of the reaction solution was withdrawn at specific time intervals (10, 20, 30, 40, 50, and 60 min) with filtering. The recovered solution was filtered through a 0.22 μm filter and diluted to the standard curve concentration range with deionized water. The residual concentration was then detected at 356 nm using a UV–visible spectrophotometer (UV-2700; Shimadzu, Kyoto, Japan).

Additionally, (1) the impacts of inorganic anions (Cl<sup>-</sup>, NO<sub>3</sub><sup>-</sup>, H<sub>2</sub>PO<sub>4</sub><sup>-</sup>, and CO<sub>3</sub><sup>2-</sup>), which are frequently present in natural water, were investigated in this work at a particular concentration of TC solution, a certain mass of catalyst, and a given molar mass of PDS solution. (2) Different concentrations of EtOH, TBA, and BQ were used as quenchers to study their effects on the oxidative degradation of TC.

## 3. Results and Discussion

### 3.1. Synthesis and Characterization of MoS<sub>2</sub>/MXene

According to our previous reports, MXene is prone to oxidation at high temperatures and has poor stability features, which limits its use to some extent [28]. In this study, MXene, MoS<sub>2</sub>, and MoS<sub>2</sub>/MXene nanomaterials were prepared under the same conditions, and it can be seen from the SEM image in Figure 2a that the MXene surface was oxidized at a high temperature, and a significant amount of TiO<sub>2</sub> grew on the surface of the initially smooth MXene sheet [21]. The pure MoS<sub>2</sub> nanosheets were connected in clusters and dispersed in a petal-like pattern in all directions, as shown in Figure 2b,c. The SEM images of MoS<sub>2</sub>/MXene at different magnifications are presented in Figure 2d–f. It was observed that numerous MoS<sub>2</sub> nanoflowers were uniformly growing on the MXene surface. With further magnification, it could be clearly observed that an intercalation structure between MoS<sub>2</sub> and MXene was formed, and the disappearance of TiO<sub>2</sub> particles on the MXene surface suggested that the addition of MoS<sub>2</sub> partially shielded the oxidation of MXene. The EDX mapping image of MoS<sub>2</sub>/MXene is displayed in Figure 2g, and the results showed that

the elements C, O, Mo, S, and Ti were uniformly distributed. The results of the elemental composition analysis via EDX spectroscopy are shown in Table S1. It was determined that the atomic ratio of Mo to S was about 1:2, suggesting effective synthesis of MoS<sub>2</sub>, and the high contents of C and O indicated the possibility of the presence of abundant organic functional groups. The SEM results indicated that MoS<sub>2</sub>/MXene composite materials with a stable 3D intercalation structure were successfully prepared.

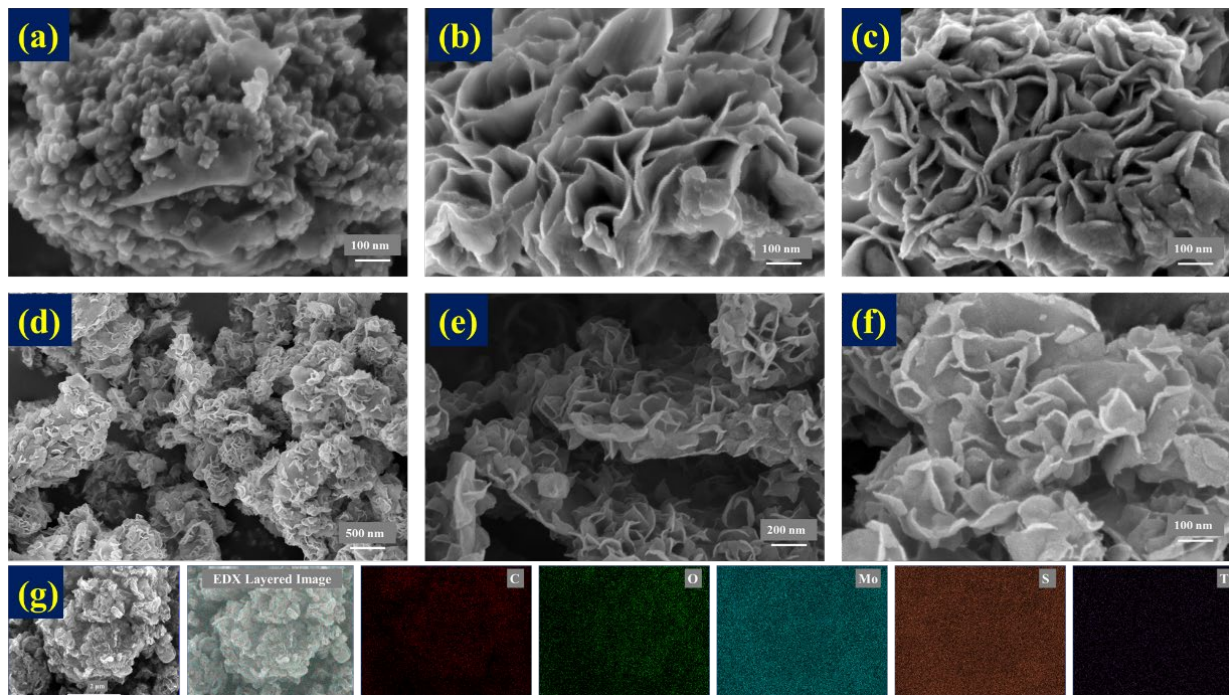


**Figure 2.** SEM images of (a) MXene, (b,c) MoS<sub>2</sub>, and (d–f) MoS<sub>2</sub>/MXene at different magnifications, and (g) EDX electron microscope scan images and elemental distribution.

As shown in Figure 3a, after being exposed to high temperatures, MXene exhibited a broad absorption peak at 3300–3500 cm<sup>-1</sup> and a significant absorption peak at 450–530 cm<sup>-1</sup>, which were attributed to the stretching vibration of the O-H single bond and the Ti-O-Ti bond, respectively [31]. It indicated that the MXene surface was readily oxidized to generate TiO<sub>2</sub> under high temperatures. Additionally, the disappearance of the characteristic peak of the Ti-O-Ti bond was observed in the FTIR chart of MoS<sub>2</sub>/MXene, indicating that MoS<sub>2</sub> could serve as a reactive oxygen barrier for MXene and shield it from oxidation at high temperatures [32]. The characteristic peak at 2926 cm<sup>-1</sup> was due to -CH<sub>3</sub> stretching [33]. The characteristic peaks at 1055, 1123, 1541, and 1629 cm<sup>-1</sup> were assigned to the stretching vibrations of the C-N, C-O, N-H, and C=O bonds of the EDTA fraction attached to the MoS<sub>2</sub> surface, respectively [34]. Furthermore, the peaks at 765 and 596 cm<sup>-1</sup> corresponded to out-of-plane C-H bond bending and S-S bond stretching, respectively, due to bond formation between the S atoms of MoS<sub>2</sub> and DDC [35]. The characteristic peak at 457 cm<sup>-1</sup> was associated with S-Mo stretching, indicating the successful formation of MoS<sub>2</sub> nanostructures [29,36]. Apparently, MoS<sub>2</sub>/MXene possesses more functional groups and surface-active sites, which are potentially more conducive to the effective activation of PDS for the degradation of various refractory organics.

To further investigate the chemical state and composition of the synthesized MoS<sub>2</sub>/MXene nanocomplexes and to identify the functional group species, an XPS examination was performed. As shown in the measured spectra (Figure 3b), the peaks at 532.2, 456.1, 285.1, 228.4, and 161.8 eV corresponded to O 1s, Ti 2p, C 1s, Mo 3d, and S 2p, respectively [29,37]. The results showed that MoS<sub>2</sub> and MXene were successfully combined, which is consistent with the findings of the SEM and FTIR analyses. In addition, in the high-resolution spectrum

of C1s (Figure 3c), the peaks at 281.4 eV, 284.8 eV, 286.4 eV, and 288.8 eV corresponded to Ti-C, C-C, C-O, and O-C=O, respectively [38]. In the O1s high-resolution spectrum (Figure 3d), the peaks at 529.7 eV, 532.0 eV, and 533.6 eV were associated with Ti-O, C-OH, and C=O, respectively [39]. All of these characterization findings suggested that there were several functional groups on the composite surface. In the Mo 3d spectrum (Figure 3e), the double peaks had lower binding energies (231.5 and 228.3 eV), which were associated with  $\text{Mo}^{4+} 3d_{3/2}$  and  $3d_{5/2}$  of  $\text{MoS}_2$ , respectively, and the weak characteristic peaks at 233.1 and 235.6 eV were caused by the presence of trace quantities of unreduced  $\text{Mo}^{6+}$  [29,40]. Additionally, the peak detected at 225.3 eV could be attributed to the S 2s signal [20]. In the S 2p spectrum (Figure 3f), the obtained double peaks of S  $2p_{3/2}$  and S  $2p_{1/2}$  at  $\sim 161.0$  and  $\sim 162.2$  eV were attributed to the  $\text{S}^{2-}$  of  $\text{MoS}_2$  [29]. These analytical test findings showed that  $\text{MoS}_2$  and  $\text{MoS}_2/\text{MXene}$  with plenty of edge active sites were successfully prepared.

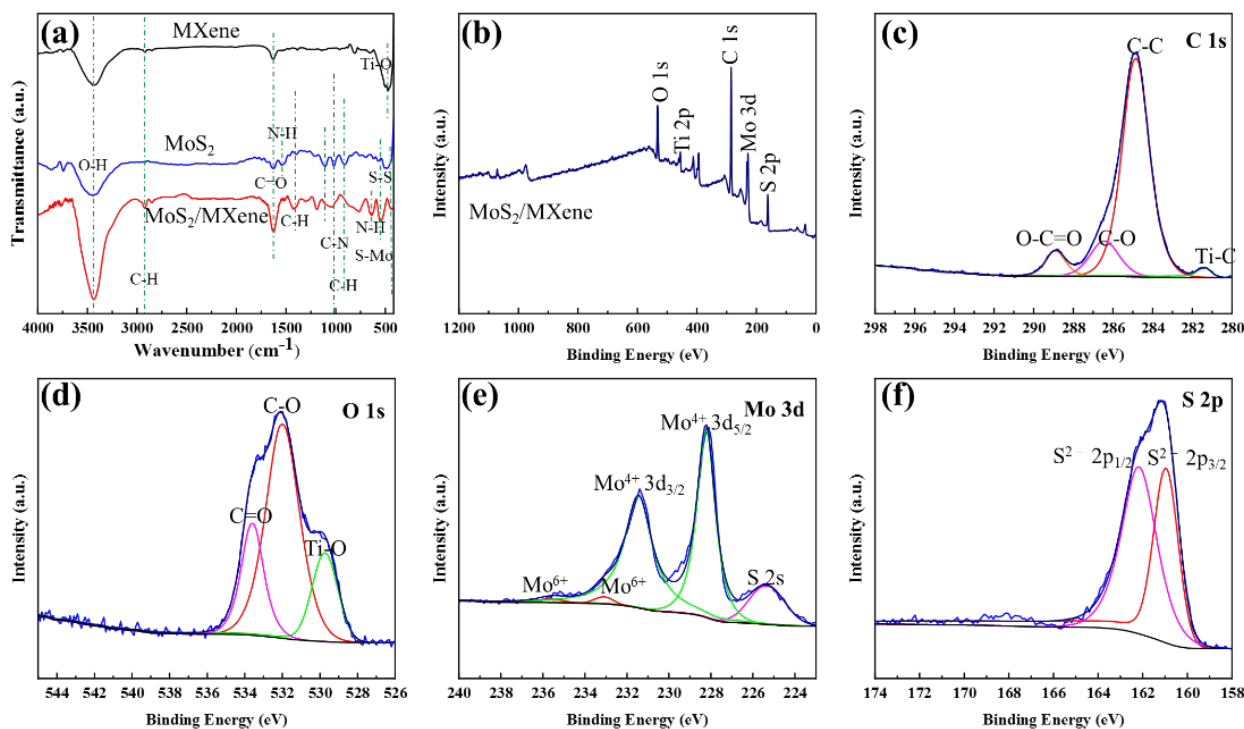


**Figure 3.** (a) FTIR spectra of MXene,  $\text{MoS}_2$ , and  $\text{MoS}_2/\text{MXene}$ ; (b) XPS survey spectra of  $\text{MoS}_2/\text{MXene}$ , (c) C 1s, (d) O 1s, and (e) Mo 3d; and (f) S 2p spectra of  $\text{MoS}_2/\text{MXene}$ .

### 3.2. Performance Regarding TC Degradation

The effects of different materials and systems, catalyst dosage, PDS consumption, pH, and initial concentration of TC on its degradation were investigated, and the results are shown in Figure 4.

Since the best TC removal effect was obtained when the mass ratio of  $\text{MoS}_2$  to MXene was 3:1, the composites with this mass ratio were used in subsequent experiments (Figure S1). As shown in Figure S1, when MXene or  $\text{MoS}_2$  was present alone, the degradation efficiency of TC was limited (41.28% and 55.56%, respectively), while the degradation efficiency of TC became higher (75.30%) when  $\text{MoS}_2/\text{MXene}$  was used.

As shown in Figure 4a, the effects of different materials or systems on TC degradation were studied under the same catalyst dosage or PDS concentration conditions. In the presence of PDS alone for 1 h, the degradation efficiency of TC was poor (18.07%), while the addition of MXene or  $\text{MoS}_2$  accelerated the degradation efficiency of TC (71.82% and 74.06%, respectively). More interestingly, the inclusion of  $\text{MoS}_2/\text{MXene}$  significantly accelerated the degradation of TC, which could achieve 100% efficiency at around 50 min. In addition, it can be inferred from Figure S2 that all four systems conformed to the

pseudo-first-order kinetic equations when degrading TC, and the parameters are listed in Table S2. These results imply that the vertical development of MoS<sub>2</sub> on MXene exposes more active sites, thus enhancing electron mobility across the composites and promoting the rapid degradation of TC [41].

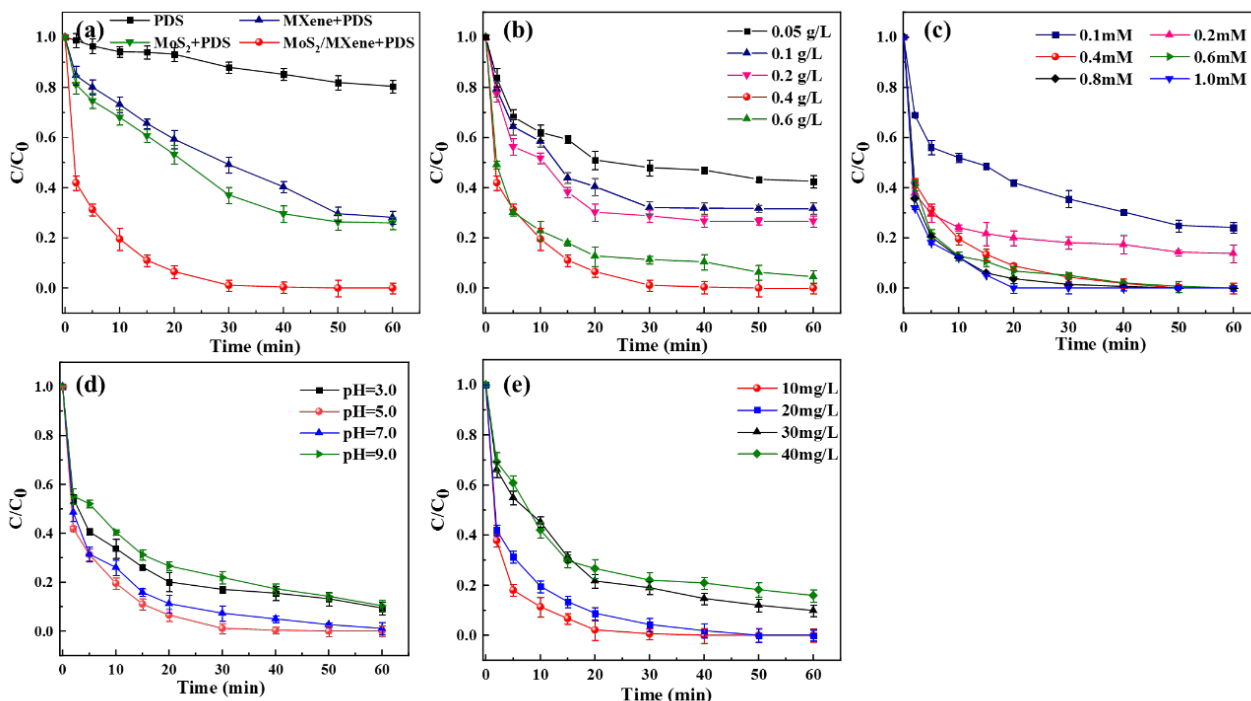


**Figure 4.** Effects of different factors on TC degradation: (a) material system; (b) catalyst dosage; (c) PDS concentration; (d) pH; and (e) TC initial concentration.

The impacts of different dosages of catalyst and PDS concentrations on TC degradation were also investigated, and the results are displayed in Figure 2b,c. The TC degradation efficiency improved significantly from 57.45% to 100% within 1 h of the process as the catalyst dosage rose from 0.05 g/L to 0.4 g/L. This was attributed to an increase in the rate of production of  $\bullet\text{OH}$  and other reactive oxygen species (ROS) inside the reaction system as the MoS<sub>2</sub>/MXene concentration increased. However, despite the increase in catalyst dosage, the degradation efficiency of TC did not improve considerably. This could probably be attributed to the limited number of active sites on the catalyst [42]. Additionally, at a catalyst dosage of 0.4 g/L, the impact of varying PDS concentrations on TC removal was investigated. The rate of TC degradation exhibited a general trend toward improvement as the PDS concentration increased (75.88%  $\rightarrow$  100%). It might be attributed to an increase in the concentration of PDS in the MoS<sub>2</sub>/MXene/PDS system, which promoted the excitation of  $\text{S}_2\text{O}_8^{2-}$  by MoS<sub>2</sub>/MXene to form  $\text{SO}_4^{\bullet-}$  while also producing more active species, thereby efficiently catalyzing the breakdown of TC in the solution [43].

Similarly, the effectiveness of TC degradation was also influenced by the initial pH of the reaction system. As shown in Figure 4d, the degradation efficiency of TC under weakly acidic and neutral circumstances was greater than that under acidic and weakly basic conditions. When the initial pH was raised from 3.0 to 5.0, the degradation efficiency of TC rose from 90.56% to 100%, but as the pH was increased further from 7 to 9, the degradation efficiency was inhibited at a rate of 1.09% and 10.36%, respectively. This may be explained by the fact that TC in an aqueous solution occurs as cations under an acidic environment, whereas the MoS<sub>2</sub>/MXene surface is readily protonated and positively charged, which causes their mutual exclusion and reduces the effectiveness of removing TC [44]. Moreover, the difference in TC degradation efficiency may be attributed to the fact that when the initial pH is too low, a considerable quantity of  $\text{H}^+$  in the solution will form hydrogen bonds

with the O-O group in  $S_2O_8^{2-}$ , which negatively impacts PDS activation or is associated with the autolytic degradation of  $HSO_5^{\bullet-}$  and the generation of  $SO_5^{\bullet-}$  [45,46]. On the other hand, TC is more easily adsorbed on the surface of the catalyst in weakly acidic or neutral conditions, leading to a higher PDS activation efficiency, and thus, improving the degradation efficiency [47]. In contrast, because TC in an aqueous solution exists as anions under alkaline circumstances and the material's surface protonation is impaired, its adsorption is diminished, and a considerable amount of  $OH^-$  in the solution competes with TC molecules, thereby limiting their removal [48]. In addition, the impact of the initial concentration of TC was investigated. The results clearly showed that when the initial concentration of TC increased, its degradation efficiency dropped since increasing the initial concentration in the reaction system meant more reactive oxygen species (ROS) were present for catalytic degradation [49].

To further explore the action pattern of  $\bullet OH$  production by  $MoS_2/MXene$  nanoparticles during TC degradation, ESR was employed to detect the DMPO- $\bullet OH$  signal intensity, and the results are shown in Figure 5. It was demonstrated that  $MoS_2/MXene$  nanoparticles generated significantly more  $\bullet OH$  in acidic air than in neutral or basic air (Figure 5a–c). Due to the intermolecular polarization of  $MoS_2$ , the  $MoS_2/MXene$  nanocomposite created a piezoelectric potential to stimulate the breakdown of water molecules to form  $\bullet OH$ , which was accelerated at higher  $H^+$  concentrations [50]. The results clearly demonstrated that  $MoS_2/MXene$  could produce  $\bullet OH$  autonomously in exposed aqueous solutions. Additionally, the intensity peak of DMPO- $\bullet OH$  dropped with an increase in solution pH, showing the strongest signal peak at pH = 4.0 compared to other solution pH values (7.0 and 9.0). The intensity of the DMPO- $\bullet OH$  signal is shown in Figure 5d,e, when MXene and  $MoS_2$  were employed as an independent catalyst, respectively. The results revealed that under the same circumstances, the intensity of the DMPO- $\bullet OH$  signal was significantly lower than that of the  $MoS_2/MXene$  nanocomposite when only MXene or  $MoS_2$  was present. Therefore, it could be inferred that the formation of particular heterojunctions between  $MoS_2$  and MXene enhanced the nanocomposite's ability to transmit electrons, thus promoting the generation of  $\bullet OH$  [41,51], which potentially stimulated PDS activation and enhanced TC degradation in turn.

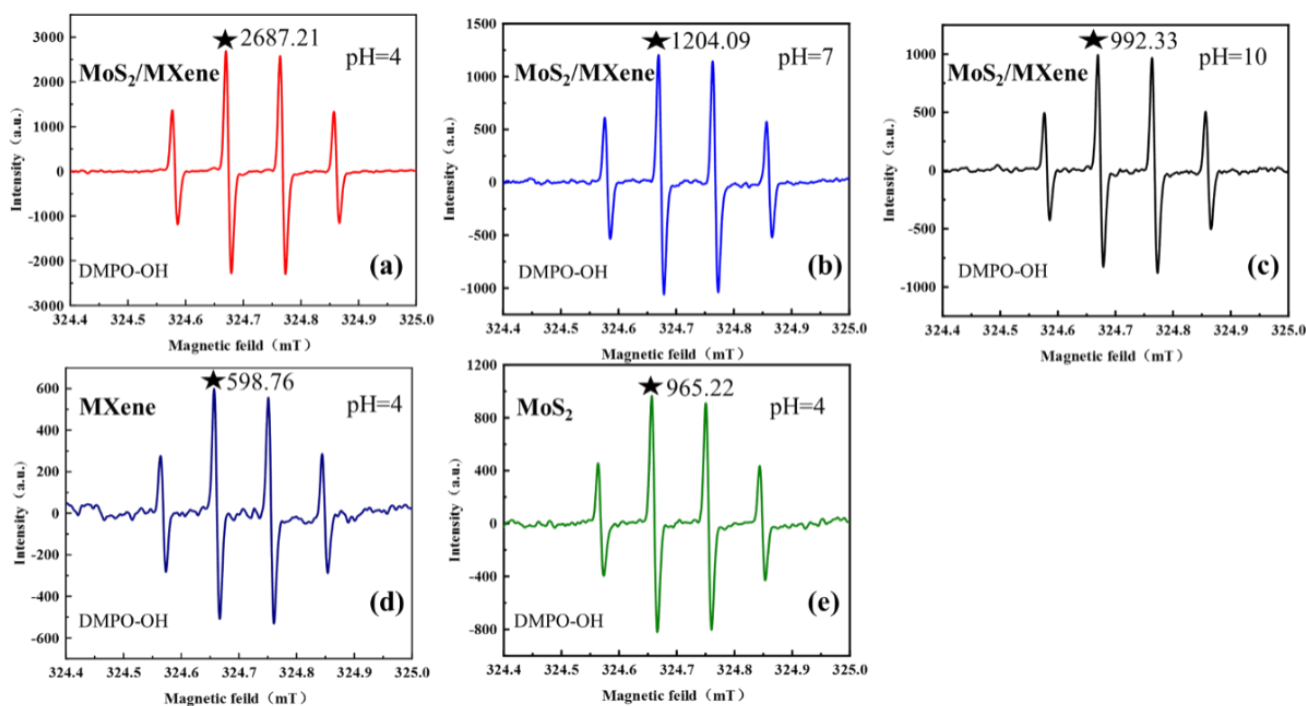


**Figure 5.** Intensity of DMPO- $\bullet OH$  signals in the presence of (a–c)  $MoS_2/MXene$ , pH = 4, 7, or 9; (d)  $Ti_3C_2$  MXene, pH = 4; and (e)  $MoS_2$ , pH = 4.

### 3.3. Effect of Inorganic Anions

The impacts of inorganic anions ( $\text{Cl}^-$ ,  $\text{NO}_3^-$ ,  $\text{H}_2\text{PO}_4^-$ , and  $\text{CO}_3^{2-}$ ), which are frequently present in natural water, were investigated in this work. As shown in Figure 6a, a relatively low concentration (0.5 mM) of  $\text{Cl}^-$  could significantly reduce the removal efficiency of TC. Moreover, increasing the concentration of  $\text{Cl}^-$  from 0.5 mM to 1.0 mM enhanced the degradation efficiency of TC, although a further increase would restrict the degradation efficiency. This is probably due to the fact that  $\text{Cl}^-$  at low concentrations would combine rapidly with  $\text{SO}_4^{\bullet-}$  to form  $\text{SO}_4^{2-}$ , which would hinder the degradation of TC in an aqueous solution, whereas higher concentrations might generate other active species such as  $\text{Cl}^\bullet$  and  $\text{Cl}_2^\bullet$ , which might stimulate TC breakdown (Equations (1) and (2)) [52]. However, when the concentration of  $\text{Cl}^-$  was gradually increased to 20 mM, various active species were depleted, and some inorganic compounds were generated in the system (Equation (3)) [53]. Therefore, the degrading efficiency of TC was slightly impacted.

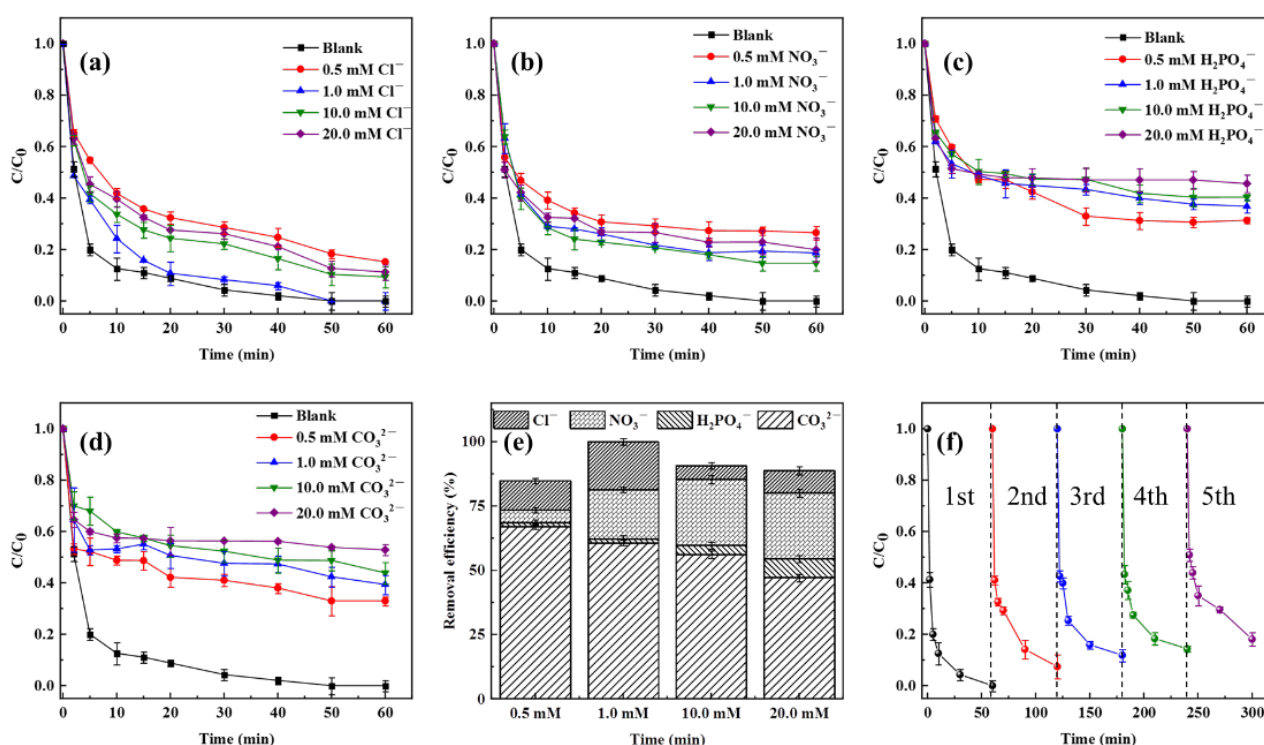
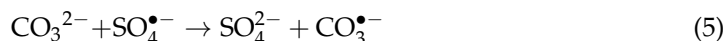
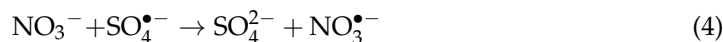
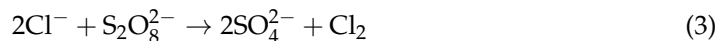


**Figure 6.** (a–e) Effects of different inorganic anions on the MoS<sub>2</sub>/MXene/PDS system, and (f) the degradation of TC in the recycling study of the MoS<sub>2</sub>/MXene/PDS system.

Similarly, when the concentration of  $\text{NO}_3^-$  was raised from 0.5 mM to 10 mM, the degradation of TC reduced from 26.55% to 14.66% (Figure 6b), which could be attributed to the generation of  $\text{NO}_3^\bullet$  (Equation (4)) [54]. However, when the concentration of  $\text{NO}_3^-$  was increased further, the degradation rate of TC reduced, which might be related to the conversion of various highly active chemicals into less active or inactive ones in the system.

In contrast, the degradation rate of TC decreased with an increase in the concentrations of  $\text{H}_2\text{PO}_4^-$  and  $\text{CO}_3^{2-}$  (Figure 6c,d), which might be due to the scavenging action of these inorganic anions on  $\text{SO}_4^{\bullet-}$  (Equations (5)–(10)) [55]. Overall, as shown in Figure 6e, the order of the inhibition effect of inorganic anions was  $\text{CO}_3^{2-} > \text{H}_2\text{PO}_4^- > \text{NO}_3^- > \text{Cl}^-$ , which was essentially consistent with the conclusions of previous studies [56].





### 3.4. Reusability Assessment of MoS<sub>2</sub>/MXene

In real application areas, the reusability of a catalyst is a crucial factor. The degradation rate of TC in the MoS<sub>2</sub>/MXene/PDS system served as an indication for repeated experiments using the catalysts. We conducted five tests with repeated cycles using the MoS<sub>2</sub>/MXene/PDS system. At the end of each cycle, MoS<sub>2</sub>/MXene was sonicated after being evenly distributed in a certain volume of ultrapure water. After natural sedimentation and centrifugation, the remaining concentration of TC in the supernatant was determined. Then, the preceding stages were repeated until there was no residual TC precipitated from the filtrate. Finally, the completely processed MoS<sub>2</sub>/MXene was dried overnight in a vacuum oven at 60 °C and ground to powder for the following cycle. As shown in Figure 6f, the removal rate of TC decreased steadily from 100% to 81.92% with an increase in cycle number. It can be inferred that MoS<sub>2</sub>/MXene is sufficiently reusable for the degradation of organic contaminants. Furthermore, the decreased performance might be due to a minor overflow of catalytic units contained in the catalyst [54]. The catalyst might also adsorb certain degradation intermediates, thus limiting the degradation effectiveness of TC [56]. Therefore, MoS<sub>2</sub>/MXene is practicable as an effective system for degrading TC by activating PDS, with some potential reusability.

### 3.5. Activation Mechanism of MoS<sub>2</sub>/MXene/PDS System

The distinct functions of reactive oxygen species generated in the MoS<sub>2</sub>/MXene/PDS system were investigated by employing free radical capture experiments. Some common scavengers and their rate constants are listed in Table S3; ethanol (EtOH), tert-butyl alcohol (TBA), and p-benzoquinone (BQ) were chosen as the scavengers of SO<sub>4</sub><sup>•−</sup>, •OH, and O<sub>2</sub><sup>•−</sup>, respectively, for comparing their reaction constants [57]. As shown in Figure 7, different scavengers impacted the degradation efficiency of TC to varying degrees under the 1 mM addition condition. The inhibitory impact of EtOH in the MoS<sub>2</sub>/MXene/PDS system became apparent within the first 10 min of the reaction, demonstrating that SO<sub>4</sub><sup>•−</sup> produced by the activation of PDS via MoS<sub>2</sub>/MXene was primarily accountable for the degradation of TC in the primary phase of the reaction. The effect of TBA became increasingly apparent as the reaction continued, suggesting that when most of the PDS was engaged in the MoS<sub>2</sub>/MXene/PDS system, further degradation of TC depended on •OH generated by MoS<sub>2</sub>/MXene in the aqueous solution. The effectiveness of TC removal by EtOH and TBA decreased from 100% to 83.89% and 77.59%, respectively, after one hour of the reaction, demonstrating that SO<sub>4</sub><sup>•−</sup> and •OH were partially responsible for TC degradation. Additionally, the degradation efficiency of TC was somewhat reduced after BQ was introduced. After the reaction had proceeded for one hour, the degradation efficiency of TC reduced from 100% to 85.68%, indicating that O<sub>2</sub><sup>•−</sup> was extremely likely involved in the process. According to the results of the free radical capture experiments, it can be inferred that various reactive oxygen species play a significant role in the degradation of TC in the MoS<sub>2</sub>/MXene/PDS system, whose effect is in the order of •OH > SO<sub>4</sub><sup>•−</sup> > O<sub>2</sub><sup>•−</sup>. Moreover, the non-significant inhibition further indicated the great stability and high efficiency of

the MoS<sub>2</sub>/MXene/PDS system, as well as its potential for having outstanding adsorption capabilities in addition to acting as a catalyst for PDS activation.

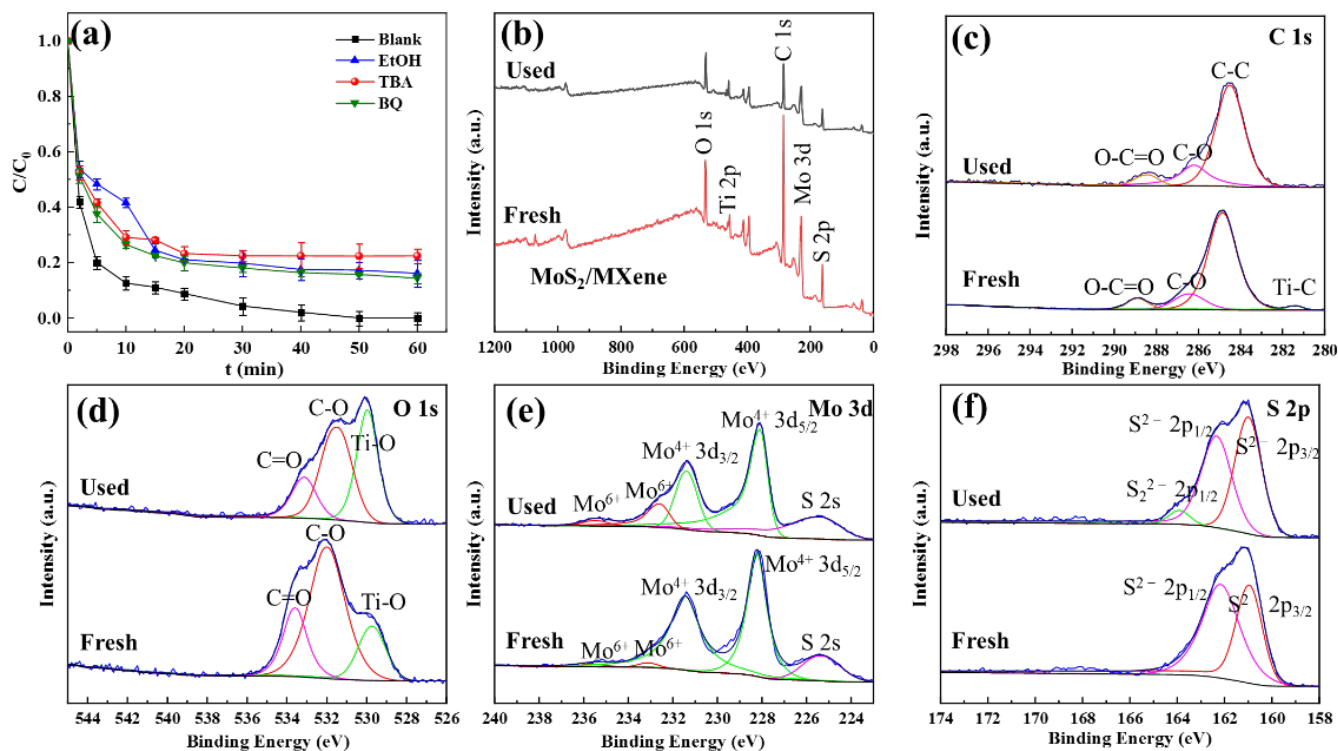
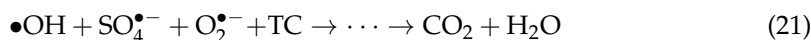
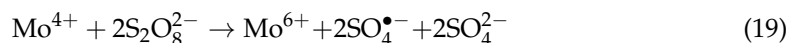
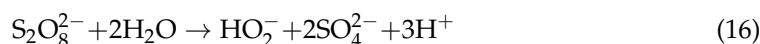
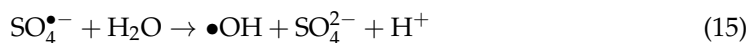
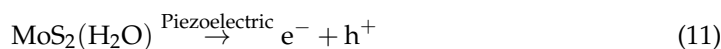


**Figure 7.** (a) Effects of different free radical bursting agents; (b) the XPS survey spectra of fresh and used MoS<sub>2</sub>/MXene, (c) C 1s, (d) O 1s, and (e) Mo 3d; and (f) S 2p spectra of fresh and used MoS<sub>2</sub>/MXene.

To further explore the surface-active sites involved in the reaction, the elemental changes in both fresh and used MoS<sub>2</sub>/MXene, including valence and content, were characterized utilizing XPS analysis. As shown in Figure 7b, the peaks at 530.9, 458.7, 284.8, 228.4, and 161.9 eV corresponded to O 1s, Ti 2p, C 1s, Mo 3d, and S 2p, respectively. There was no significant change in the location or content of these peaks, indicating that MoS<sub>2</sub>/MXene possessed good stability (Table S4). Moreover, the high-resolution XPS spectra of C 1s, O 1s, Mo 3d, and S 2p are displayed in Figure 7c–f. As seen in Table S5, the Mo<sup>6+</sup> concentration increased from 0.07% to 0.86% after the reaction, whereas the Mo<sup>4+</sup> content decreased from 5.93% to 4.54%, demonstrating that the slight oxidation of Mo<sup>4+</sup> on the surface is a major factor for PDS activation. It is worth noting that the slight decrease in Mo<sup>4+</sup> content might be attributed to the interconversion of Mo<sup>4+</sup> and Mo<sup>6+</sup> [58]. Additionally, the Ti-O content increased from 5.61% to 8.57%, demonstrating that MXene and MoS<sub>2</sub> were possibly engaged in the activation process of PDS and that their combined action could efficiently speed up this process. Meanwhile, the contents of C-O and C=O groups reduced from 16.52% and 5.93% to 9.88% and 3.99%, respectively. It was further revealed that both C-O and C=O groups were necessary for the activation of PDS and the generation of reactive oxygen species [59]. More interestingly, in the high-resolution XPS pattern of S, a novel signal peak at 164.0 eV was discovered, which was identified as bridging S<sub>2</sub><sup>2-</sup> at the apical of MoS<sub>2</sub>, suggesting a potential linkage reaction between pure MoS<sub>2</sub> and further indicating the involvement of MoS<sub>2</sub> in the oxidation reaction [60].

A suggested mechanism of PDS activation by MoS<sub>2</sub>/MXene for effective TC degradation was proposed after combining the above findings and analyses. Due to the combined piezoelectric and semiconducting properties of MoS<sub>2</sub>, effective removal of organic dyes could be accomplished in the dark (termed piezoelectric catalysis) [61]. A strong hydrogen peak was still detected in the solution after the removal of MoS<sub>2</sub>, which was likely due to

the extended existence of a high concentration of  $\bullet\text{OH}$  in the aqueous solution containing  $\text{MoS}_2$  [50]. This finding is also highly consistent with the results of the ESR detection. Therefore, the following equations (Equations (11)–(21)) were derived to account for the ROS generated during the oxidative degradation of TC, as well as the chemical reactions in the  $\text{MoS}_2/\text{MXene}/\text{PDS}$  system, based on the experimental findings and previous reports [42,50,56,58,59]. Specifically, in the initial phase of oxidative degradation, electrons and holes are formed due to the piezoelectric catalysis and internal polarization of  $\text{MoS}_2$ , which will stimulate the polarization decomposition of water molecules to produce  $\bullet\text{OH}$ , and the above processes can be accelerated in acidic solutions exposed to air. Then, the high concentration of  $\bullet\text{OH}$  promotes  $\text{SO}_4^{2-}$  to generate  $\text{SO}_4^{\bullet-}$  in the aqueous solution, which rapidly attaches to organic molecules and triggers their oxidative breakdown [62]. Moreover, PDS can produce weak  $\text{SO}_4^{\bullet-}$  and  $\text{O}_2^{\bullet-}$  in an aqueous solution, while  $\text{MoS}_2$  can expedite this process and permit cyclic redox, considerably enhancing the utilization of the catalyst. Finally, TC is mineralized by a variety of ROS into different small molecules such as  $\text{H}_2\text{O}$  and  $\text{CO}_2$ .



### 3.6. Possible Degradation Pathways

To further clarify the degradation mechanism of TC, liquid chromatography–mass spectrometry (LC-MS) was used to identify the intermediates present in the  $\text{MoS}_2/\text{MXene}/\text{PDS}$  system at different times. Figure S3 and Table S6 show the  $m/z$  values and supposed structure of TC degradation intermediates at different times in the presence of the  $\text{MoS}_2/\text{MXene}$  catalyst, and signal peaks with different  $m/z$  values can be observed for these intermediates. Based on the LC-MS data and previous reports, three possible degradation pathways of TC were proposed (Figure 8). In pathway I, the original TC molecule ( $m/z = 446$ ) is converted to intermediate P11 ( $m/z = 460$ ) via dehydration, which is followed by deamidation and dealkylation to yield intermediate P12 ( $m/z = 374$ ). It is then converted to intermediates P13 ( $m/z = 302$ ) and P14 ( $m/z = 242$ ) through oxidative ring-opening reaction and gradual decarbonylation. Finally, these intermediates are further oxidized to small molecules P15 ( $m/z = 240$ ), P16 ( $m/z = 220$ ), P17 ( $m/z = 228$ ), and P18 ( $m/z = 99$ ). In pathway II, the original TC molecule is first converted to intermediate P21 ( $m/z = 416$ ) via demethylation. It then undergoes a dealkylation reaction to produce P22 ( $m/z = 376$ ), and further deamidation and ring-opening reactions produce intermediate P23 ( $m/z = 338$ ). Finally, it gradually forms small organic molecules via decarbonylation and oxidation reactions. Alternatively, P21 is slowly converted to other small molecules, namely, P24 ( $m/z = 360$ ), P25 ( $m/z = 211$ ), and P26 ( $m/z = 121$ ), via progressive oxidation. In pathway III, the original TC molecule is first dehydrated and converted to intermediate P31 ( $m/z = 427$ ). It can then undergo demethylation, dealkylation, and ring-opening reactions to produce P32 ( $m/z = 319$ ). With further oxidation, other organics, namely, P33 ( $m/z = 279$ ),

P34 ( $m/z = 207$ ), and P35 ( $m/z = 181$ ), can be formed. Moreover, P31 can form intermediate P36 ( $m/z = 301$ ) via a ring-opening reaction on the left side and hydroxylation and then intermediate P37 ( $m/z = 274$ ) via deamidation. Finally, with further oxidative degradation, it can be transformed into intermediates P38 ( $m/z = 131$ ) and P39 ( $m/z = 112$ ). When  $\text{MoS}_2/\text{MXene}$  is present in the system, TC can eventually be mineralized into inorganic substances, such as  $\text{CO}_2$  and  $\text{H}_2\text{O}$ , with the oxidation of various ROS.

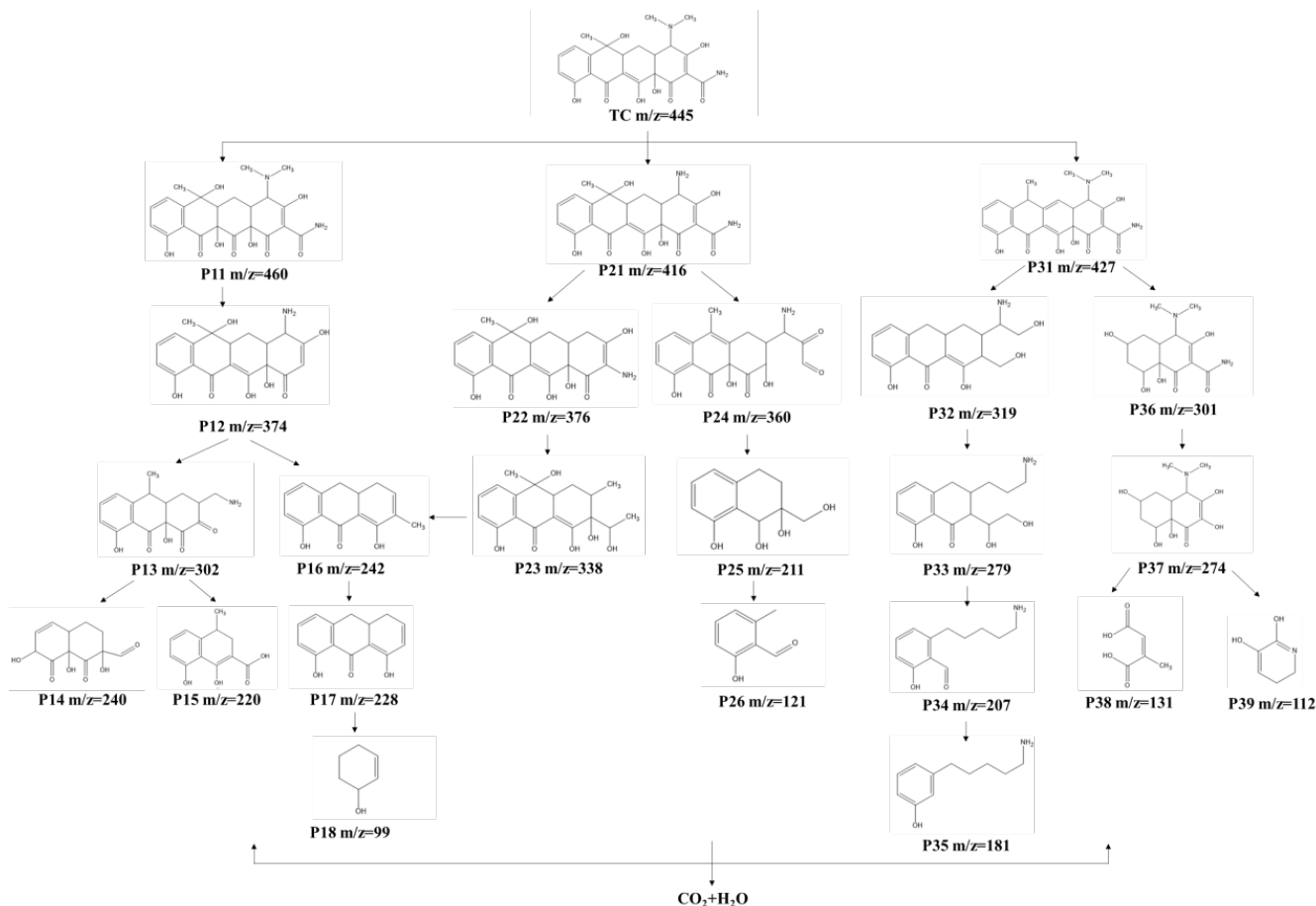


**Figure 8.** Possible degradation pathways of TC.

#### 4. Conclusions

In this study,  $\text{MoS}_2/\text{MXene}$  nanocomplexes were prepared in a simple one-step hydrothermal approach utilizing  $\text{Ti}_3\text{C}_2$  MXene as a substrate, which was employed as an effective catalyst for the activation of PDS to effectively degrade TC. The characterization of  $\text{MoS}_2/\text{MXene}$  was carried out using SEM, FTIR, and XPS, and it was observed that a stable 3D intercalation structure was formed through the self-assembly of  $\text{MoS}_2$  with MXene under solvent heat. This not only resulted in an expanded layer spacing and increased the number of surface-active sites for the catalyst, but it also successfully prevented MXene from being oxidized at high temperatures and inhibited  $\text{MoS}_2$  from clustering. More interestingly,  $\text{MoS}_2/\text{MXene}$  performed better catalytically than individual MXene and  $\text{MoS}_2$ , implying that tight contact between  $\text{MoS}_2$  and MXene occurred. The  $\bullet\text{OH}$  produced was crucial in the activation of PDS and the oxidative destruction of TC when  $\text{MoS}_2/\text{MXene}$  was present in the aqueous solutions, particularly in acidic solutions. In addition, TC could be completely removed in about 50 min under the conditions of a catalyst dosage of 0.4 g/L, a PDS concentration of 0.4 mM, and pH = 5.0 at room temperature. Despite the interference of various inorganic anions, TC was removed from the  $\text{MoS}_2/\text{MXene}/\text{PDS}$  system relatively successfully. Through repeated testing, the recyclability of  $\text{MoS}_2/\text{MXene}$  was assessed, and the catalyst was shown to have excellent reusability performance. Furthermore, the

mechanism of action of the MoS<sub>2</sub>/MXene/PDS system on the TC degradation process was determined by extrapolating the formation principle of ROS during the reaction process and examining the intermediates and potential degradation pathways with LC-MS. Therefore, this study demonstrated that MoS<sub>2</sub>/MXene is a promising composite catalyst for the removal and degradation of persistent organic pollutants in water, and it also expanded the application of MoS<sub>2</sub>-based, MXene-based, and MoS<sub>2</sub>/MXene composites in catalytic oxidation.

**Supplementary Materials:** The following supporting information can be downloaded at: <https://www.mdpi.com/article/10.3390/nano14090786/s1>, Figure S1 Effect of different materials on the degradation efficiency of TC. Figure S2 Kinetic fitting models for different materials/systems. Figure S3 MS full scan spectra of intermediates in TC degradation in the MoS<sub>2</sub>/MXene/PDS system by LC-MS. Table S1 The elemental weight percentages and atomic percentages of MoS<sub>2</sub>/MXene were calculated by EDX spectroscopy. Table S2 The fitting parameters of kinetic models of TC degradation by MoS<sub>2</sub>/MXene/PDS. Table S3 The reaction rate constants of radicals with the corresponding scavenger. Table S4 The Elemental peak positions and contents of fresh and used MoS<sub>2</sub>/MXene. Table S5 The group percentages of fresh and used MoS<sub>2</sub>/MXene. Table S6 Liquid-phase mass spectrometry (LC-MS) analysis of intermediates and possible structural formulae.

**Author Contributions:** Conceptualization, Y.S. and R.C.; Software, S.Y.; Formal analysis, X.N., M.F. and H.X.; Investigation, X.N.; Data curation, S.Y. and M.F.; Writing—original draft, Y.S. and S.L.; Writing—review & editing, Y.S., R.C. and H.X.; Supervision, Y.S. and R.C.; Funding acquisition, Y.S. and R.C. All authors have read and agreed to the published version of the manuscript.

**Funding:** This study received financial support from the Natural Science Foundation of Hunan Province (No. 2022JJ50259); the Scientific Research Project of Education Department of Hunan Province (No. 22B0279, No. 22A0193); the Major program Natural Science Foundation of Hunan Province of China (No. 2021JC0001); the Science and Technology Talent Support Project of Hunan Province (No. 2022TJ-Q19); the National Natural Science Foundation of China (No. 52374424); and the Environmental Research Foundation of Hunan Province of China (No. HBKT-2022010).

**Data Availability Statement:** Data are contained within the article and Supplementary Materials.

**Conflicts of Interest:** The authors declare no conflict of interest.

## References

1. Gopal, G.; Alex, S.A.; Chandrasekaran, N.; Mukherjee, A. A review on tetracycline removal from aqueous systems by advanced treatment techniques. *RSC Adv.* **2020**, *10*, 27081–27095. [[CrossRef](#)] [[PubMed](#)]
2. Li, N.; Zhou, L.; Jin, X.; Owens, G.; Chen, Z. Simultaneous removal of tetracycline and oxytetracycline antibiotics from wastewater using a ZIF-8 metal organic-framework. *J. Hazard. Mater.* **2019**, *366*, 563–572. [[CrossRef](#)] [[PubMed](#)]
3. Xin, S.; Liu, G.; Ma, X.; Gong, J.; Ma, B.; Yan, Q.; Chen, Q.; Ma, D.; Zhang, G.; Gao, M. High efficiency heterogeneous Fenton-like catalyst biochar modified CuFeO<sub>2</sub> for the degradation of tetracycline: Economical synthesis, catalytic performance and mechanism. *Appl. Catal. B Environ.* **2021**, *280*, 119386. [[CrossRef](#)]
4. Park, J.; Yamashita, N.; Park, C.; Shimono, T.; Takeuchi, D.M.; Tanaka, H. Removal characteristics of pharmaceuticals and personal care products: Comparison between membrane bioreactor and various biological treatment processes. *Chemosphere* **2017**, *179*, 347–358. [[CrossRef](#)] [[PubMed](#)]
5. Cao, J.; Lai, L.; Lai, B.; Yao, G.; Chen, X.; Song, L. Degradation of tetracycline by peroxymonosulfate activated with zero-valent iron: Performance, intermediates, toxicity and mechanism. *Chem. Eng. J.* **2019**, *364*, 45–56. [[CrossRef](#)]
6. Huang, D.; Zhang, G.; Yi, J.; Cheng, M.; Lai, C.; Xu, P.; Zhang, C.; Liu, Y.; Zhou, C.; Xue, W. Progress and challenges of metal-organic frameworks-based materials for SR-AOPs applications in water treatment. *Chemosphere* **2021**, *263*, 127672. [[CrossRef](#)] [[PubMed](#)]
7. Gao, L.; Mao, Q.; Luo, S.; Cao, L.; Xie, X.; Yang, Y.; Deng, Y.; Wei, Z. Experimental and theoretical insights into kinetics and mechanisms of hydroxyl and sulfate radicals-mediated degradation of sulfamethoxazole: Similarities and differences. *Environ. Pollut.* **2020**, *259*, 113795. [[CrossRef](#)] [[PubMed](#)]
8. Yin, R.; Guo, W.; Wang, H.; Du, J.; Zhou, X.; Wu, Q.; Zheng, H.; Chang, J.; Ren, N. Enhanced peroxymonosulfate activation for sulfamethazine degradation by ultrasound irradiation: Performances and mechanisms. *Chem. Eng. J.* **2018**, *335*, 145–153. [[CrossRef](#)]
9. Duan, X.; Sun, H.; Kang, J.; Wang, Y.; Indrawirawan, S.; Wang, S. Insights into heterogeneous catalysis of persulfate activation on dimensional-structured nanocarbons. *ACS Catal.* **2015**, *5*, 4629–4636. [[CrossRef](#)]
10. Anipsitakis, G.P.; Dionysiou, D.D. Radical generation by the interaction of transition metals with common oxidants. *Environ. Sci. Technol.* **2004**, *38*, 3705–3712. [[CrossRef](#)] [[PubMed](#)]
11. Zhou, H.; Lai, L.; Wan, Y.; He, Y.; Yao, G.; Lai, B. Molybdenum disulfide (MoS<sub>2</sub>): A versatile activator of both peroxymonosulfate and persulfate for the degradation of carbamazepine. *Chem. Eng. J.* **2020**, *384*, 123264. [[CrossRef](#)]

12. Wang, J.; Wang, S. Activation of persulfate (PS) and peroxymonosulfate (PMS) and application for the degradation of emerging contaminants. *Chem. Eng. J.* **2018**, *334*, 1502–1517. [[CrossRef](#)]
13. Ji, Y.; Dong, C.; Kong, D.; Lu, J. New insights into atrazine degradation by cobalt catalyzed peroxymonosulfate oxidation: Kinetics, reaction products and transformation mechanisms. *J. Hazard. Mater.* **2015**, *285*, 491–500. [[CrossRef](#)]
14. Giannakis, S.; Lin, K.-Y.A.; Ghanbari, F. A review of the recent advances on the treatment of industrial wastewaters by Sulfate Radical-based Advanced Oxidation Processes (SR-AOPs). *Chem. Eng. J.* **2021**, *406*, 127083. [[CrossRef](#)]
15. Ma, D.; Yi, H.; Lai, C.; Liu, X.; Huo, X.; An, Z.; Li, L.; Fu, Y.; Li, B.; Zhang, M. Critical review of advanced oxidation processes in organic wastewater treatment. *Chemosphere* **2021**, *275*, 130104. [[CrossRef](#)] [[PubMed](#)]
16. Sheng, B.; Yang, F.; Wang, Y.; Wang, Z.; Li, Q.; Guo, Y.; Lou, X.; Liu, J. Pivotal roles of MoS<sub>2</sub> in boosting catalytic degradation of aqueous organic pollutants by Fe (II)/PMS. *Chem. Eng. J.* **2019**, *375*, 121989. [[CrossRef](#)]
17. Chen, Y.; Zhang, G.; Liu, H.; Qu, J. Confining free radicals in close vicinity to contaminants enables ultrafast fenton-like processes in the interspacing of MoS<sub>2</sub> membranes. *Angew. Chem. Int. Ed.* **2019**, *58*, 8134–8138. [[CrossRef](#)]
18. Liu, C.; Kong, D.; Hsu, P.-C.; Yuan, H.; Lee, H.-W.; Liu, Y.; Wang, H.; Wang, S.; Yan, K.; Lin, D. Rapid water disinfection using vertically aligned MoS<sub>2</sub> nanofilms and visible light. *Nat. Nanotechnol.* **2016**, *11*, 1098–1104. [[CrossRef](#)]
19. Ai, K.; Ruan, C.; Shen, M.; Lu, L. MoS<sub>2</sub> nanosheets with widened interlayer spacing for high-efficiency removal of mercury in aquatic systems. *Adv. Funct. Mater.* **2016**, *26*, 5542–5549. [[CrossRef](#)]
20. Yang, S.; Liu, Q.; Wan, X.; Jiang, J.; Ai, L. Edge-rich MoS<sub>2</sub> nanosheets anchored on layered Ti<sub>3</sub>C<sub>2</sub> MXene for highly efficient and rapid catalytic reduction of 4-nitrophenol and methylene blue. *J. Alloys Compd.* **2022**, *891*, 161900. [[CrossRef](#)]
21. Li, X.; Lv, X.; Sun, X.; Yang, C.; Zheng, Y.-Z.; Yang, L.; Li, S.; Tao, X. Edge-oriented, high-percentage 1T'-phase MoS<sub>2</sub> nanosheets stabilize Ti<sub>3</sub>C<sub>2</sub> MXene for efficient electrocatalytic hydrogen evolution. *Appl. Catal. B Environ.* **2021**, *284*, 119708. [[CrossRef](#)]
22. Naguib, M.; Kurtoglu, M.; Presser, V.; Lu, J.; Niu, J.; Heon, M.; Hultman, L.; Gogotsi, Y.; Barsoum, M.W. Two-dimensional nanocrystals produced by exfoliation of Ti<sub>3</sub>AlC<sub>2</sub>. *Adv. Mater.* **2011**, *23*, 4248–4253. [[CrossRef](#)] [[PubMed](#)]
23. Seh, Z.W.; Fredrickson, K.D.; Anasori, B.; Kibsgaard, J.; Strickler, A.L.; Lukatskaya, M.R.; Gogotsi, Y.; Jaramillo, T.F.; Vojvodic, A. Two-dimensional molybdenum carbide (MXene) as an efficient electrocatalyst for hydrogen evolution. *ACS Energy Lett.* **2016**, *1*, 589–594. [[CrossRef](#)]
24. Habib, T.; Zhao, X.; Shah, S.A.; Chen, Y.; Sun, W.; An, H.; Lutkenhaus, J.L.; Radovic, M.; Green, M.J. Oxidation stability of Ti<sub>3</sub>C<sub>2</sub>T<sub>x</sub> MXene nanosheets in solvents and composite films. *NPJ 2D Mater. Appl.* **2019**, *3*, 8. [[CrossRef](#)]
25. Navitski, I.; Ramanaviciute, A.; Ramanavicius, S.; Pogorielov, M.; Ramanavicius, A. MXene-Based Chemo-Sensors and Other Sensing Devices. *Nano-Mater.* **2024**, *14*, 447. [[CrossRef](#)] [[PubMed](#)]
26. Adomavičiūtė-Grabusovė, S.; Ramanavičius, S.; Popov, A.; Šablinskas, V.; Gogotsi, O.; Ramanavičius, A. Selective enhancement of SERS spectral bands of salicylic acid adsorbate on 2D Ti<sub>3</sub>C<sub>2</sub>T<sub>x</sub>-based MXene film. *Chemosensors* **2021**, *9*, 223. [[CrossRef](#)]
27. Sarycheva, A.; Gogotsi, Y. Raman Spectroscopy Analysis of the Structure and Surface Chemistry of Ti<sub>3</sub>C<sub>2</sub>T<sub>x</sub> MXene. *Chem. Mater.* **2020**, *32*, 3480–3488. [[CrossRef](#)]
28. Chen, R.; Cheng, Y.; Wang, P.; Wang, Y.; Wang, Q.; Yang, Z.; Tang, C.; Xiang, S.; Luo, S.; Huang, S. Facile synthesis of a sandwiched Ti<sub>3</sub>C<sub>2</sub>T<sub>x</sub> MXene/nZVI/fungal hypha nanofiber hybrid membrane for enhanced removal of Be (II) from Be (NH<sub>2</sub>)<sub>2</sub> complexing solutions. *Chem. Eng. J.* **2021**, *421*, 129682. [[CrossRef](#)]
29. Kumar, N.; Fosso-Kankeu, E.; Ray, S.S. Achieving controllable MoS<sub>2</sub> nanostructures with increased interlayer spacing for efficient removal of Pb (II) from aquatic systems. *ACS Appl. Mater. Interfaces* **2019**, *11*, 19141–19155. [[CrossRef](#)] [[PubMed](#)]
30. Gogotsi, Y.; Anasori, B. The rise of MXenes. *ACS Nano* **2019**, *13*, 8491–8494. [[CrossRef](#)] [[PubMed](#)]
31. Othman, Z.; Sinopoli, A.; Mackey, H.R.; Mahmoud, K.A. Efficient Photocatalytic Degradation of Organic Dyes by AgNPs/TiO<sub>2</sub>/Ti<sub>3</sub>C<sub>2</sub>T<sub>x</sub> MXene Composites under UV and Solar Light. *ACS Omega* **2021**, *6*, 33325–33338. [[CrossRef](#)] [[PubMed](#)]
32. Mao, X.; Zou, Y.; Xu, F.; Sun, L.; Chu, H.; Zhang, H.; Zhang, J.; Xiang, C. Three-dimensional self-supporting Ti<sub>3</sub>C<sub>2</sub> with MoS<sub>2</sub> and Cu<sub>2</sub>O nanocrystals for high-performance flexible supercapacitors. *ACS Appl. Mater. Interfaces* **2021**, *13*, 22664–22675. [[CrossRef](#)] [[PubMed](#)]
33. Wang, Y.; Zheng, K.; Zhan, W.; Huang, L.; Liu, Y.; Li, T.; Yang, Z.; Liao, Q.; Chen, R.; Zhang, C. Highly effective stabilization of Cd and Cu in two different soils and improvement of soil properties by multiple-modified biochar. *Ecotoxicol. Environ. Saf.* **2021**, *207*, 111294. [[CrossRef](#)] [[PubMed](#)]
34. Zhang, X.; Yang, S.; Yu, B.; Tan, Q.; Zhang, X.; Cong, H. Advanced modified polyacrylonitrile membrane with enhanced adsorption property for heavy metal ions. *Sci. Rep.* **2018**, *8*, 1260. [[CrossRef](#)]
35. Li, L.; Qu, Q.; Bai, W.; Yang, F.; Chen, Y.; Zhang, S.; Ding, Z. Sodium diethyldithiocarbamate as a corrosion inhibitor of cold rolled steel in 0.5 M hydrochloric acid solution. *Corros. Sci.* **2012**, *59*, 249–257. [[CrossRef](#)]
36. Wang, Z.; Mi, B. Environmental applications of 2D molybdenum disulfide (MoS<sub>2</sub>) nanosheets. *Environ. Sci. Technol.* **2017**, *51*, 8229–8244. [[CrossRef](#)] [[PubMed](#)]
37. Hwang, S.K.; Kang, S.-M.; Rethinasabapathy, M.; Roh, C.; Huh, Y.S. MXene: An emerging two-dimensional layered material for removal of radioactive pollutants. *Chem. Eng. J.* **2020**, *397*, 125428. [[CrossRef](#)]
38. Liu, C.; Zhang, H.; Li, R.; Li, X.; Tang, P.; Wang, Y.; Yang, B.; Qiao, Z.; Yang, G. Laser triggered exothermic chemical reaction in Au nanoparticle@Ti<sub>3</sub>C<sub>2</sub> MXene membrane: A route toward efficient light to high-temperature pulse conversion. *Chem. Eng. J.* **2021**, *420*, 127672. [[CrossRef](#)]
39. Tang, T.; Yin, Z.; Chen, J.; Zhang, S.; Sheng, W.; Wei, W.; Xiao, Y.; Shi, Q.; Cao, S. Novel pn heterojunction Bi<sub>2</sub>O<sub>3</sub>/Ti<sup>3+</sup>-TiO<sub>2</sub> photocatalyst enables the complete removal of tetracyclines under visible light. *Chem. Eng. J.* **2021**, *417*, 128058. [[CrossRef](#)]

40. Liu, J.; Jia, Z.; Zhou, W.; Liu, X.; Zhang, C.; Xu, B.; Wu, G. Self-assembled MoS<sub>2</sub>/magnetic ferrite CuFe<sub>2</sub>O<sub>4</sub> nanocomposite for high-efficiency microwave absorption. *Chem. Eng. J.* **2022**, *429*, 132253. [[CrossRef](#)]
41. Jiao, S.; Liu, L. Friction-induced enhancements for photocatalytic degradation of MoS<sub>2</sub>@Ti<sub>3</sub>C<sub>2</sub> nanohybrid. *Ind. Eng. Chem. Res.* **2019**, *58*, 18141–18148. [[CrossRef](#)]
42. Wang, Y.; Ji, Q.; Xu, J.; Wan, J.; Wang, L. Activation of peroxydisulfate using N-doped carbon-encapsulated Ni species for efficient degradation of tetracycline. *Sep. Purif. Technol.* **2021**, *276*, 119369. [[CrossRef](#)]
43. He, D.; Zhu, K.; Huang, J.; Shen, Y.; Lei, L.; He, H.; Chen, W. N, S co-doped magnetic mesoporous carbon nanosheets for activating peroxymonosulfate to rapidly degrade tetracycline: Synergistic effect and mechanism. *J. Hazard. Mater.* **2022**, *424*, 127569. [[CrossRef](#)] [[PubMed](#)]
44. Wang, P.; Yap, P.-S.; Lim, T.-T. C-N-S tridoped TiO<sub>2</sub> for photocatalytic degradation of tetracycline under visible-light irradiation. *Appl. Catal. A Gen.* **2011**, *399*, 252–261. [[CrossRef](#)]
45. Du, W.; Zhang, Q.; Shang, Y.; Wang, W.; Li, Q.; Yue, Q.; Gao, B.; Xu, X. Sulfate saturated biosorbent-derived Co-S@NC nanoarchitecture as an efficient catalyst for peroxymonosulfate activation. *Appl. Catal. B Environ.* **2020**, *262*, 118302. [[CrossRef](#)]
46. He, J.; Wan, Y.; Zhou, W. ZIF-8 derived Fe-N coordination moieties anchored carbon nanocubes for efficient peroxymonosulfate activation via non-radical pathways: Role of FeN<sub>x</sub> sites. *J. Hazard. Mater.* **2021**, *405*, 124199. [[CrossRef](#)] [[PubMed](#)]
47. Wang, Y.; Zhang, H.; Chen, L. Ultrasound enhanced catalytic ozonation of tetracycline in a rectangular air-lift reactor. *Catal. Today* **2011**, *175*, 283–292. [[CrossRef](#)]
48. Yang, L.; Shengwang, G.; Lijun, W.; Jianchao, Z.; Hong, G.; Xunfeng, X. Tetracycline degradation in aqueous solution by porous MoS<sub>2</sub>/g-C<sub>3</sub>N<sub>4</sub>. *Chin. J. Environ. Eng.* **2019**, *13*, 818–825.
49. Gao, Y.; Chen, Z.; Zhu, Y.; Li, T.; Hu, C. New insights into the generation of singlet oxygen in the metal-free peroxymonosulfate activation process: Important role of electron-deficient carbon atoms. *Environ. Sci. Technol.* **2019**, *54*, 1232–1241. [[CrossRef](#)] [[PubMed](#)]
50. Wu, J.M.; Sun, Y.-G.; Chang, W.-E.; Lee, J.-T. Piezoelectricity induced water splitting and formation of hydroxyl radical from active edge sites of MoS<sub>2</sub> nanoflowers. *Nano Energy* **2018**, *46*, 372–382. [[CrossRef](#)]
51. Hou, W.; Sun, Y.; Zhang, Y.; Wang, T.; Wu, L.; Du, Y.; Zhong, W. Mixed-dimensional heterostructure of few-layer MXene based vertical aligned MoS<sub>2</sub> nanosheets for enhanced supercapacitor performance. *J. Alloys Compd.* **2021**, *859*, 157797. [[CrossRef](#)]
52. Ao, X.; Liu, W.; Sun, W.; Cai, M.; Ye, Z.; Yang, C.; Lu, Z.; Li, C. Medium pressure UV-activated peroxymonosulfate for ciprofloxacin degradation: Kinetics, mechanism, and genotoxicity. *Chem. Eng. J.* **2018**, *345*, 87–97. [[CrossRef](#)]
53. Peng, L.; Shang, Y.; Gao, B.; Xu, X. Co<sub>3</sub>O<sub>4</sub> anchored in N, S heteroatom co-doped porous carbons for degradation of organic contaminant: Role of pyridinic N-Co binding and high tolerance of chloride. *Appl. Catal. B Environ.* **2021**, *282*, 119484. [[CrossRef](#)]
54. Gao, Y.; Zou, D. Efficient degradation of levofloxacin by a microwave-3D ZnCo<sub>2</sub>O<sub>4</sub>/activated persulfate process: Effects, degradation intermediates, and acute toxicity. *Chem. Eng. J.* **2020**, *393*, 124795. [[CrossRef](#)]
55. Hu, L.; Zhang, G.; Liu, M.; Wang, Q.; Wang, P. Enhanced degradation of Bisphenol A (BPA) by peroxymonosulfate with Co<sub>3</sub>O<sub>4</sub>-Bi<sub>2</sub>O<sub>3</sub> catalyst activation: Effects of pH, inorganic anions, and water matrix. *Chem. Eng. J.* **2018**, *338*, 300–310. [[CrossRef](#)]
56. Liu, Z.; Gao, Z.; Wu, Q. Activation of persulfate by magnetic zirconium-doped manganese ferrite for efficient degradation of tetracycline. *Chem. Eng. J.* **2021**, *423*, 130283. [[CrossRef](#)]
57. Pu, M.; Wan, J.; Zhang, F.; Brusseau, M.L.; Ye, D.; Niu, J. Insight into degradation mechanism of sulfamethoxazole by metal-organic framework derived novel magnetic Fe@C composite activated persulfate. *J. Hazard. Mater.* **2021**, *414*, 125598. [[CrossRef](#)]
58. Zhu, Y.; Wang, F.; Zhou, B.; Chen, H.; Yuan, R.; Zhang, Y.; Geng, H.; Liu, Y.; Wang, H. Photo-assisted Fe<sup>2+</sup> modified molybdenum disulfide activated potassium persulfate to degrade sulfadiazine: Insights into the degradation pathway and mechanism from density functional theory. *Chem. Eng. J.* **2022**, *435*, 134904. [[CrossRef](#)]
59. Yang, Y.; Ji, W.; Li, X.; Lin, H.; Chen, H.; Bi, F.; Zheng, Z.; Xu, J.; Zhang, X. Insights into the mechanism of enhanced peroxymonosulfate degraded tetracycline using metal organic framework derived carbonyl modified carbon-coated Fe<sup>0</sup>. *J. Hazard. Mater.* **2022**, *424*, 127640. [[CrossRef](#)] [[PubMed](#)]
60. Cao, P.; Peng, J.; Liu, S.; Cui, Y.; Hu, Y.; Chen, B.; Li, J.; Zhai, M. Tuning the composition and structure of amorphous molybdenum sulfide/carbon black nanocomposites by radiation technique for highly efficient hydrogen evolution. *Sci. Rep.* **2017**, *7*, 16048. [[CrossRef](#)] [[PubMed](#)]
61. Liu, S.; Jing, B.; Nie, C.; Ao, Z.; Duan, X.; Lai, B.; Shao, Y.; Wang, S.; An, T. Piezoelectric activation of peroxymonosulfate by MoS<sub>2</sub> nanoflowers for the enhanced degradation of aqueous organic pollutants. *Environ. Sci. Nano* **2021**, *8*, 784–794. [[CrossRef](#)]
62. Yao, Y.; Cai, Y.; Lu, F.; Wei, F.; Wang, X.; Wang, S. Magnetic recoverable MnFe<sub>2</sub>O<sub>4</sub> and MnFe<sub>2</sub>O<sub>4</sub>-graphene hybrid as heterogeneous catalysts of peroxymonosulfate activation for efficient degradation of aqueous organic pollutants. *J. Hazard. Mater.* **2014**, *270*, 61–70. [[CrossRef](#)]

**Disclaimer/Publisher's Note:** The statements, opinions and data contained in all publications are solely those of the individual author(s) and contributor(s) and not of MDPI and/or the editor(s). MDPI and/or the editor(s) disclaim responsibility for any injury to people or property resulting from any ideas, methods, instructions or products referred to in the content.